ACCURATE 3D VISCOUS INCOMPRESSIBLE FLOW CALCULATIONS WITH THE FEM

Ü. GÜLÇAT* AND A. R. ASLAN

Faculty of Aeronautics and Astronautics, Istanbul Technical University, 80626 Maslak, Istanbul, Turkey

SUMMARY

A second-order-accurate (in both time and space) formulation is developed and implemented for solution of the three-dimensional incompressible Navier–Stokes equations involving high-Reynolds-number flows past complex configurations. For stabilization, only a fourth-order-accurate artificial dissipation term in the momentum equations is used. The finite element method (FEM) with an explicit time-marching scheme based on two-fractional-step integration is used for solution of the momentum equations. The element-by-element (EBE) technique is employed for solution of the auxiliary potential function equation in order to ease the memory requirements for matrix. The cubic cavity problem, the laminar flow past a sphere at various Reynolds numbers and the flow around the fuselage of a helicopter are successfully solved. Comparison of the results with the low-order solutions indicates that the flow details are depicted clearly even with coarse grids. © 1997 John Wiley & Sons, Ltd.

1. INTRODUCTION

Numerical solution of the three-dimensional Navier–Stokes equations has received considerable attention over the past two decades. For a numerical technique to respond to the demands of current developments, however, the scheme involved must be high-order-accurate, fast and efficient as far as memory requirements and computing times are concerned.

Recent advances in iterative solution techniques have enabled CFD researchers to solve large-scale problems in acceptable computation times with the fast processors of the 1990s. These iterative solvers have become convenient CFD tools since they do not require excessive computer memories for either implicit time-marching schemes or inversion of elliptic equations. For finite element computations, element-by-element (EBE) iteration schemes demand the least amount of memory. In this connection the conjugate gradient (CG) method becomes an efficient and fast-converging iterative method when applied with preconditioning (PCG) to the discrete form of the equations.[1–3]

In this study a second-order accurate (in both time and space) scheme is developed and

---

* Correspondence to: Ü. Gülçat, Faculty of Aeronautics and Astronautics, Istanbul Technical University, 80626 Maslak, Istanbul, Turkey.

implemented for solution of the three-dimensional incompressible Navier–Stokes equations involving high-Reynolds-number laminar flows about complex configurations. To do this, a fourth-order-accurate artificial dissipation term in the momentum equations is used for stabilization. The finite element method (FEM) with an explicit time-marching scheme is used for solution and the EBE technique is employed in order to ease the memory requirements for storage of the stiffness matrix of the FEM.[3] Since the scheme is time-accurate, the transient nature of the flow field is properly resolved.

For calibration of the code, firstly the cubic cavity problem is solved. The comparison with the existing literature where spectral methods are employed[4] is satisfactory even with quite a coarse grid. Then, for further calibration of the code, low-Reynolds-number ($Re = 100$ and 200) flows past a sphere are solved. After the calibration studies the flow past a sphere at a subcritical Reynolds number, $Re = 162,000$, is studied. The recirculating flow features are depicted properly. Finally, to test the capabilities of the code, the flow past a generic helicopter fuselage is solved. The flow features and the aerodynamic forces are predicted satisfactorily.

All the computations are performed on a dedicated host machine equipped with an i860 processor with 32 MB of memory on board.

2. FORMULATION

Starting from the Navier–Stokes equations, a new formulation for a second-order time-accurate scheme is derived. First the weak formulation of the momentum equations is obtained to form the necessary integral relations. Using these integral relations and evaluating the integrand at the middle of the time step to attain second-order accuracy, the time-integrated form of the momentum equations is obtained. The spatial discretization of the equations, on the other hand, is performed using eight-node hexahedral elements with trilinear shape functions.[5] Since the flow Reynolds number is high, a fourth-order artificial viscosity term is explicitly added to the momentum equations for stabilization. The following subsections describe these formulations.

2.1. Integral formulation

The equations governing the flow of an incompressible viscous fluid are

$$\nabla \cdot \mathbf{u} = 0, \tag{1}$$

$$\frac{\partial \mathbf{u}}{\partial t} + \mathbf{u} \cdot \nabla \mathbf{u} = -\nabla p + \frac{1}{Re} \nabla^2 \mathbf{u}. \tag{2}$$

The equations are written in vector form (boldface symbols denote vector or matrix quantities). The variables are non-dimensionalized using a reference velocity and a characteristic length as usual. $Re = Ul/v$ is the Reynolds number, where U is the reference velocity, l is the characteristic length and v is the kinematic viscosity of the fluid. The velocity vector, pressure and time are denoted by $\mathbf{u}$, p and t respectively.

The weak form of equation (2) over the space–time domain reads as

$$\int_\Omega \int_t \frac{\partial \mathbf{u}}{\partial t} \cdot \mathbf{N} \, \mathrm{d}\Omega \, \mathrm{d}t = \int_\Omega \int_t \left(-\mathbf{u} \cdot \nabla \mathbf{u} - \nabla p + \frac{1}{Re} \nabla^2 \mathbf{u} \right) \cdot \mathbf{N} \, \mathrm{d}\Omega \, \mathrm{d}t, \tag{3}$$

where $\mathbf{N}$ is an arbitrary weighting function. The time integration of both sides of equation (3) for half a time step, $\Delta t/2$, from time step n to $n + \frac{1}{2}$, where the integrand of the right-hand side is evaluated at time level n, gives

$$\int_\Omega (\mathbf{u}^{n+1/2} - \mathbf{u}^n) \cdot \mathbf{N} \, \mathrm{d}\Omega = \frac{\Delta t}{2} \int_\Omega \left(-\mathbf{u} \cdot \nabla \mathbf{u} - \nabla p + \frac{1}{Re} \nabla^2 \mathbf{u} \right)^n \cdot \mathbf{N} \, \mathrm{d}\Omega. \tag{4}$$

At the intermediate time step the time integration of equation (3), where the convective and viscous terms are taken at $n + \frac{1}{2}$ and the pressure term at time level n, yields

$$\int_\Omega (\mathbf{u}^* - \mathbf{u}^n) \cdot \mathbf{N} \, \mathrm{d}\Omega = \Delta t \int_\Omega \left[-\nabla p^n + \left(-\mathbf{u} \cdot \nabla \mathbf{u} + \frac{1}{Re} \nabla^2 \mathbf{u} \right)^{n+1/2} \right] \cdot \mathbf{N} \, \mathrm{d}\Omega. \tag{5}$$

For the full time step, however, the averaged value of pressure at time levels n and $n + 1$ is used to give

$$\int_\Omega (\mathbf{u}^{n+1} - \mathbf{u}^n) \cdot \mathbf{N} \, \mathrm{d}\Omega = \Delta t \int_\Omega \left[\left(-\mathbf{u} \cdot \nabla \mathbf{u} + \frac{1}{Re} \nabla^2 \mathbf{u} \right)^{n+1/2} - \nabla \frac{p^n + p^{n+1}}{2} \right] \cdot \mathbf{N} \, \mathrm{d}\Omega. \tag{6}$$

On the other hand, taking the divergence of equation (2), expressing it in a weak form and reordering the integral on the left-hand side results in

$$\int_\Omega \nabla \cdot \left(\int_t \frac{\partial \mathbf{u}}{\partial t} \, \mathrm{d}t \right) \cdot \mathbf{N} \, \mathrm{d}\Omega = \int_\Omega \int_t \nabla \cdot \left(-\mathbf{u} \cdot \nabla \mathbf{u} - \nabla p + \frac{1}{Re} \nabla^2 \mathbf{u} \right) \cdot \mathbf{N} \, \mathrm{d}\Omega \, \mathrm{d}t. \tag{7}$$

The time integration of equation (7) at the intermediate time step, however, is

$$\int_\Omega \nabla \cdot (\mathbf{u}^* - \mathbf{u}^n) \cdot \mathbf{N} \, \mathrm{d}\Omega = \Delta t \int_\Omega \nabla \cdot \left[-\nabla p^n + \left(-\mathbf{u} \cdot \nabla \mathbf{u} + \frac{1}{Re} \nabla^2 \mathbf{u} \right)^{n+1/2} \right] \cdot \mathbf{N} \, \mathrm{d}\Omega, \tag{8}$$

while at the full step, again using the averaged pressure gives

$$\int_\Omega \nabla \cdot (\mathbf{u}^{n+1} - \mathbf{u}_n) \cdot \mathbf{N} \, \mathrm{d}\Omega = \Delta t \int_\Omega \nabla \cdot \left[\left(-\mathbf{u} \cdot \nabla \mathbf{u} + \frac{1}{Re} \nabla^2 \mathbf{u} \right)^{n+1/2} - \nabla \frac{p^n + p^{n+1}}{2} \right] \cdot \mathbf{N} \, \mathrm{d}\Omega. \tag{9}$$

Subtracting (8) from (9) and making use of the continuity equation at time levels n and $n + 1$ yields

$$\int_\Omega \nabla \cdot \mathbf{u}^* \mathbf{N} \cdot \mathrm{d}\Omega = \frac{\Delta t}{2} \int_\Omega \nabla^2 (p^{n+1} - p^n) \cdot \mathbf{N} \, \mathrm{d}\Omega. \tag{10}$$

2.2. Numerical formulation

Defining the auxiliary potential function $\phi = \Delta t(p^{n+1} - p^n)$ and choosing N as trilinear shape functions,[5] for the algebraic form of the working equations one can write equations (4) and (5) as

$$\frac{2\mathbf{M}}{\Delta t} \mathbf{V}_1^\alpha = \left[\mathbf{B}_\alpha + P_e \mathbf{C}_\alpha - \left(\frac{\mathbf{A}}{Re} + \mathbf{D} \right) \mathbf{u}_\alpha \right]^n, \tag{11}$$

$$\frac{\mathbf{M}}{\Delta t} \mathbf{V}_2^\alpha = P_e^n \mathbf{C}_\alpha + \left[\mathbf{B}_\alpha - \left(\frac{\mathbf{A}}{Re} + \mathbf{D} \right) \mathbf{u}_\alpha \right]^{n+1/2}, \tag{12}$$

where α indicates the Cartesian velocity components x, y and z. The discretized form of equation (10) reads as

$$\tfrac{1}{2}\mathbf{A}\phi = \mathbf{E}_\alpha \mathbf{u}_\alpha^*. \tag{13}$$

Finally, subtracting equation (5) from (6) and performing the integrals results in

$$\mathbf{M}\mathbf{V}_3^\alpha = \tfrac{1}{2}\mathbf{E}_\alpha \phi. \tag{14}$$

A similar formulation is also given by Webster and Townsend.[6] The element auxiliary potential ϕ_e is defined as

$$\phi_e = \frac{1}{\mathrm{vol}(\Omega_e)} \int_{\Omega_e} N_i \phi_i \, \mathrm{d}\Omega_e, \quad i = 1, \ldots, 8,$$

where Ω is the flow domain and N_i are the shape functions. In the formulation given above, $\mathbf{u}^*$ is an intermediate velocity vector field which is not solenoidal.

In equations (11)–(14), $\mathbf{M}$ is the lumped element mass matrix, $\mathbf{D}$ is the advection matrix, $\mathbf{A}$ is the stiffness matrix, $\mathbf{C}$ is the coefficient matrix for pressure, $\mathbf{B}$ is the vector due to boundary conditions and $\mathbf{E}$ is the matrix due to incompressibility, $\mathbf{V}_1, \mathbf{V}_2$ and $\mathbf{B}_3$ denote the velocity vector differences

$$\mathbf{V}_1 = \mathbf{u}^{n+1/2} - \mathbf{u}^n, \tag{15a}$$

$$\mathbf{V}_2 = \mathbf{u}^* - \mathbf{u}^n, \tag{15b}$$

$$\mathbf{V}_3 = \mathbf{u}^{n+1} - \mathbf{u}^*. \tag{15c}$$

2.3. Artificial dissipation

In the present study a fourth-order-accurate artificial dissipation term in the momentum equations is used for stabilization. The diffusion term is added explicitly to the right-hand side of equations (11) and (12). The two-dimensional formulation given in Reference 7 is here extended to three dimensions. Accordingly, the artificial viscosity term is computed in two steps at the element level. First a second-order differencing is accomplished with

$$D_i^2 = \sum_{j=1}^{8} V_j - 8V_i. \tag{16}$$

These values give the second-order distributions to cell corners i for the momentum equations. Then fourth-order distributions to cell corners are formed using the values obtained from equation (16):

$$D_i^4 = \sum_{j=1}^{8} D_j^2 - 8D_i^2. \tag{17}$$

These fourth-order viscosity terms are multiplied by a certain coefficient when added to the momentum equations. For all the Cartesian velocity components the coefficient of artificial viscosity is kept the same, $c \leqslant \tfrac{1}{24}$. No dissipation term is added to the Poisson equation for the auxiliary potential.

2.4. Boundary and initial conditions

As initial conditions, uniform freestream conditions are given for the flow domain, while the solid surface is an exception with the no-slip condition.

As boundary conditions, however, freestream conditions are imposed at the far field and fully developed flow conditions are applied at the far wake. Imposing these boundary conditions on the momentum equations (11) and (12) is quite simple, since the velocity vector differences are zero at the boundaries where the velocity vector is specified.

For the auxiliary potential, ϕ is set to zero at the far wake and $\partial\phi/\partial n$ is specified as zero on the solid surface and at the far field where freestream conditions prevail.

2.5. Solution procedure

In order to solve the flow past an arbitrary body, the equations are integrated in time with the following procedure.

Starting from the time step where u^n and p^n are given:

1. Equation (11) is solved to obtain V_1 and, using equation (15a), $u^{n+1/2}$ is determined.
2. Using $u^{n+1/2}$, V_2 is obtained from equation (12) and, implementing equation (15b), u^* is determined.
3. The auxiliary potential ϕ is obtained using u^* in equation (13).
4. With this ϕ, V_3 is determined via equation (14) and, using equation (15c), the new time level velocity field u^{n+1} is calculated. The associated pressure field p^{n+1} is determined from the old time level pressure field p^n and ϕ obtained in step 3.

The above procedure is repeated until the desired time level. The accuracy of the solution and the preconditioning for solving the auxiliary potential equation are given in detail in Reference 8.

3. RESULTS AND DISCUSSION

For calibration of the code the cubic cavity problem is solved using the first-[9] and second-order-accurate schemes. Initially the grid used is fairly coarse, $11 \times 11 \times 11$. Then solutions with finer grids, 21×21 and 31×31, are obtained. Figures 1(a) and 1(b) indicate that the second-order scheme reaches the grid-independent solution faster than the first-order scheme. The first-order scheme with second-order artificial dissipation gives low velocity gradients in the vicinity of the walls as seen in Figures 1(a) and 1(b). The second-order-accurate scheme, on the other hand, predicts the velocity profiles, even with a coarse grid, in agreement with the results given by pseudospectral methods[4] where high-order approximations are used.

Shown in Figures 1(c) and 1(d) are the symmetry plane velocity vectors obtained with the first- and second-order schemes respectively. The flow Reynolds number based on the lid velocity and cavity depth is 1000 and the dimensionless time level is 30 where the steady state is practically reached.

Then, for further calibration of the code, low-Reynolds-number ($Re = 100$ and 200) flows past a sphere are solved. The symmetric half-grid around the sphere consists of 15,425 points and 14,112 brick elements. The steady state streamline polts at $Re = 100$ and 200 are shown in Figures 2(a) and 2(b) respectively on the symmetry plane. The separation points (θ_s) and the extent of the recirculatory region (l_w/D) are seen in these plots. The present values are listed in comparison with the computational values of Rimon and Cheng[10] and the experimental values of Taneda (reproduced from References 10 and 11) in Table I. All three predictions are in close agreement, the present results being closer to the experimental ones. The computed drag coefficient values are $C_D = 1 \cdot 07$ for $Re = 100$ and $C_D = 0 \cdot 78$ for $Re = 200$. Cantaloube et al.[12] predict $C_D = 0 \cdot 76$, while the Reference 10 value is $C_D = 0 \cdot 77$ for $Re = 200$. The experimentally determined value of Allen (taken from

a) vertical centerline

b) horizontal centerline

c) Solution with first order scheme

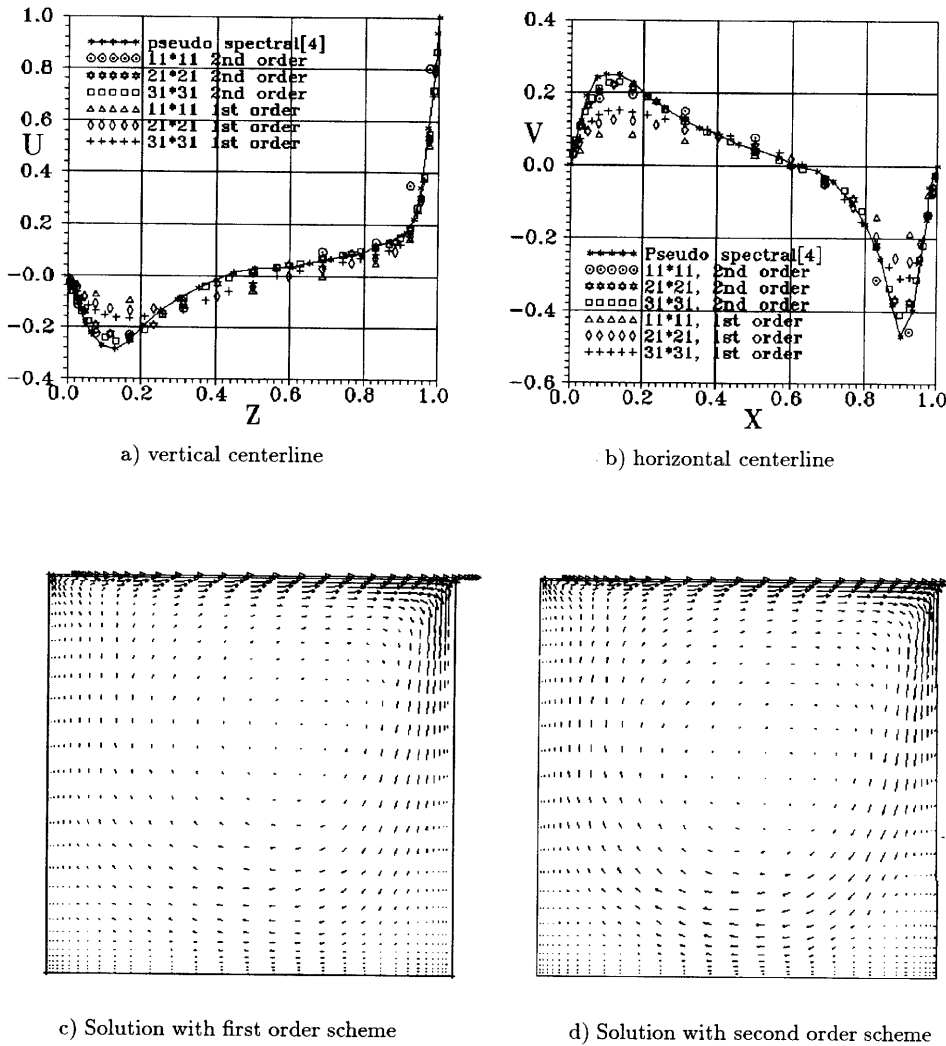d) Solution with second order scheme

Figure 1. (a, b) Cubic cavity velocity profiles for $Re = 1000$ in comparison with results of pseudospectral method[4] on symmetry plane at steady state. (c, d) Flow velocity vectors on symmetry plane. Present solutions with first- and second-order-accurate schemes are shown

Reference 11) is about $C_D = 0.8$. All these values and the values for $Re = 100$ are plotted in Figure 3. In order to observe the effect of grid size on the drag coefficient, two more computations are performed with two different grids for $Re = 100$. The sensitivity of C_D to the grid resolution is shown in Table II.

The pressure coefficient values in comparison with the axisymetric flow calculations[10] are shown in Figures 4(a) and 4(b) for $Re = 100$ and 200 respectively. There is a slight discrepancy in the wake region for $Re = 100$, while there is some discrepancy in the region where the flow accelerates ($60 < \theta < 100$, where $\theta = 0$ is the front stagnation point) for $Re = 200$. The drag coefficient variation with respect to the Reynolds number, however, shows better agreement with the experimental values as seen in Figure 3.
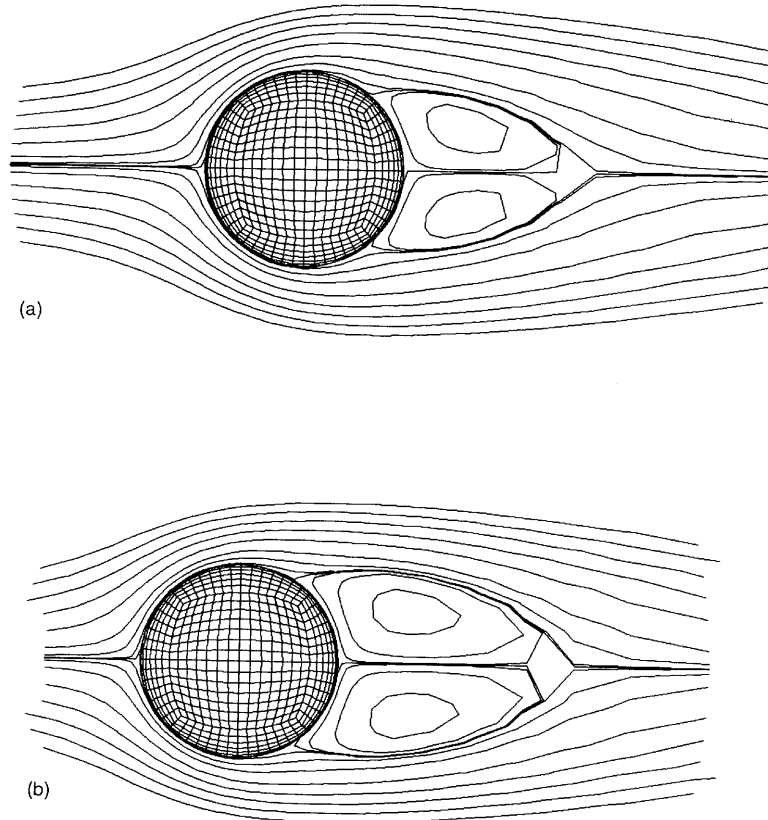
Figure 2. Steady state streamlines for flow around sphere at $Re =$ (a) 100 and (b) 200 on symmetry plane
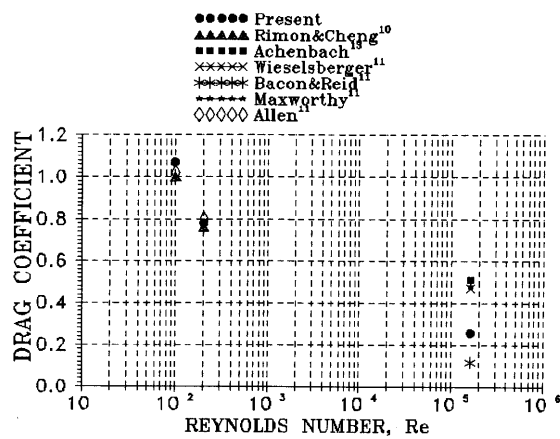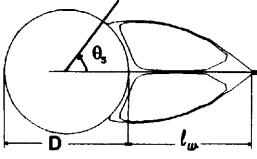

Figure 3. Computed drag coefficient (C_D) values versus Reynolds number in comparison with other numerical calculations and experimental data

Table I. Comparision of various parameters for flow about sphere with data and other computations

Re	Reference	C_D	C_{D_f}/C_D	l_w/D	θ_s (deg)
100	present	1·07	0·51	0·93	55
100	Taneda[10,11]	—	—	0·9	55
100	Rimon and Cheng[10]	1	—	0·86	53·5
100	Data[10,11]	1–1·1	—	—	—
170	Taneda[10,11]	—	—	1·12	60
200	Present	0·78	0·45	1·2	61·5
200	Rimon and Cheng[10]	0·76	—	1·06	64
200	Cantaloube et al.[12]	0·77	—	—	—
290	Taneda[10,11]	—	—	—	67
162000	Present	0·30	0·01	1·5	88
162000	Achenbach[13]	0·51	0·014	1·5	97
162000	Data[11–13]	0·12–0·51	—	—	—

As a second study the laminar flow past a sphere at a high Reynolds number, $Re = 162,000$, is solved using both the first[9] and second-order schemes. The symmetric half-grid around the sphere consists of 19,127 and 17,640 brick elements. Figures 5(a) and 5(b) show the details of the grid on the symmetry plane and around the body respectively, where in the latter case 617 points on the symmetric half of the sphere surface and 31 points in the radial direction are used. In Figures 6(a) and 6(b) the velocity vectors obtained with the first- and second-order schemes respectively at the symmetry plane at about time level $T = 4$ are plotted. The length of the vortex ring, appearing on the symmetry plane, predicted with both approaches is almost the same, but the width differs significantly. The second-order-accurate scheme predicts the maximum value of the separation angle close to the value given in Reference 13 (Table I). As seen in Figures 6(a) and 6(b), the flow appears to be symmetric with respect to the equatorial plane and in the upper half of the plane there is a major clockwise recirculating vortex. The details in the separation region, however, are predicted with the second-order-accurate scheme as seen in Figure 6(b), where a smaller vortex with clockwise rotation is present upstream of the major vortex ring. A more detailed picture of the vortex right after the shoulder is provided in Figure 7(b), where there is a very small counterclockwise rotating vortex in

Table II. Sensitivity of C_D to grid resolution for $Re = 100$

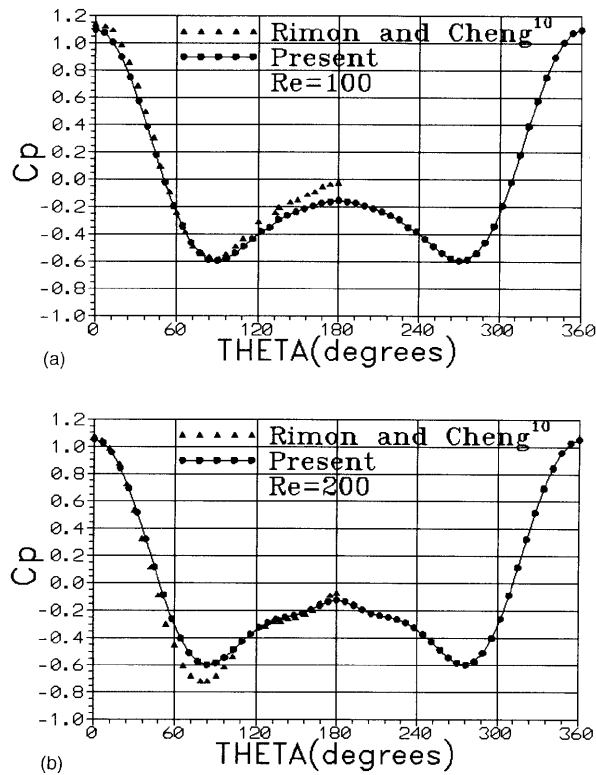| Grid	Distance from surface $\Delta r_{surface}$	C_D
Fine	0·0203	1·07
Medium	0·0336	1·04
Coarse	0·0589	0·98

Figure 4. Pressure coefficient (C_p) values in comparison with axisymmetric flow calculations[10] for $Re = (a)$ 100 and (b) 200

between the major and minor clockwise rotating vortices. All these details are smeared out with the first-order method as seen in Figure 7(a), even with finer resolution in the radial direction. The solution is carried out to further time levels to see the vortex shedding behind the sphere.

In Figures 8(a) and 8(b) the calculated streamline patterns are shown on the symmetry plane (x–y plane) and on the equatorial plane (x–z plane) respectively at the dimensionless time level $T = 17$, where the symmetry is weakened as compared with the earlier time levels. The details of the primary and secondary vortices rotating in the same direction and a smaller counter-rotating vortex are depicted clearly on the symmetry plane. On the equatorial plane, however, only the presence of the primary vortex is apparent. This indicates that at that instant, small vortices cannot stretch from the upper to the lower shoulder of the cylinder. The natural start of the vortex shedding, without any artificial disturbances, is observed in Figure 9, where streamlines are drawn at $T = 21.4$ on the symmetry plane (x–y plane). The calculated drag coefficient value is $C_D = 0.28$ and the lift coefficient value is $C_L = 0.18$ at that instant.

The comparison between the calculated and experimental surface pressure coefficient distributions on the symmetry plane is given in Figure 10. The calculated pressure values are not symmetric at the given instant $T = 21.4$ and the lower surface pressure distribution agrees well with the experimental data,[13] just provided for half of the sphere, before the shoulder. In the recirculation region, however, the appearance of secondary vortices is more pronounced with the present calculations than predicted by experiment. The ratio of the friction force (C_{D_f}) to the total drag (C_D) on the sphere is also given in Table I.
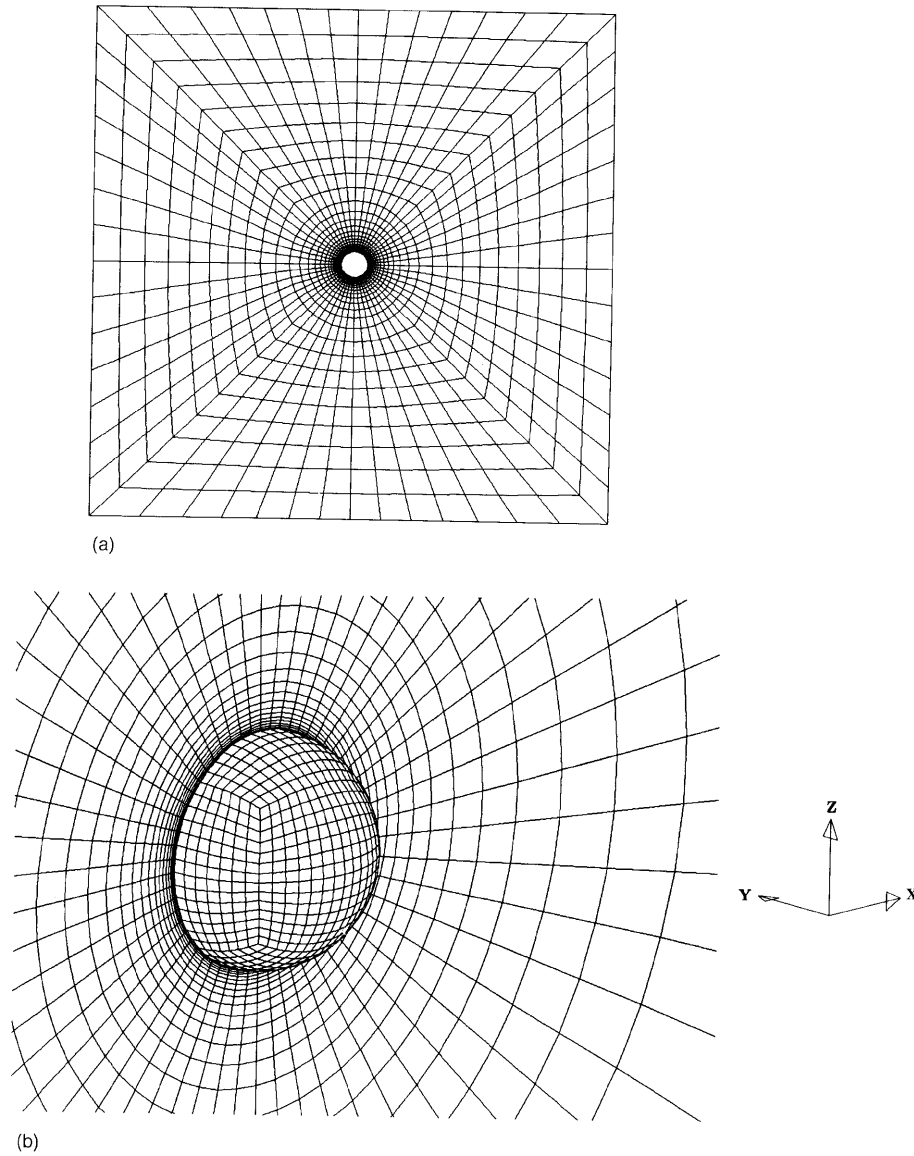
Figure 5. (a) Grid around sphere on symmetry plane. (b) Details of grid around body where 617 points on symmetric half of sphere surface and 31 points in radial direction are used. $Re = 162{,}000$

The final problem solved is related to an institutional project for designing a generic helicopter. The grid around the fuselage is shown in Figures 11(a) and 11(b), where 11,280 brick elements with 12,915 nodes are used to resolve the symmetric half of the flow field. The flow Reynolds number based on the height of the body (taken as the characteristic length) is 50,000, which corresponds to low-speed forward flight of the helicopter. Shown in Figures 12(a) and 12(b) are the symmetry plane streamline plots at about the steady state obtained with the first- and second-order schemes respectively. The results of the second-order scheme indicate a longer separation region in the wake.
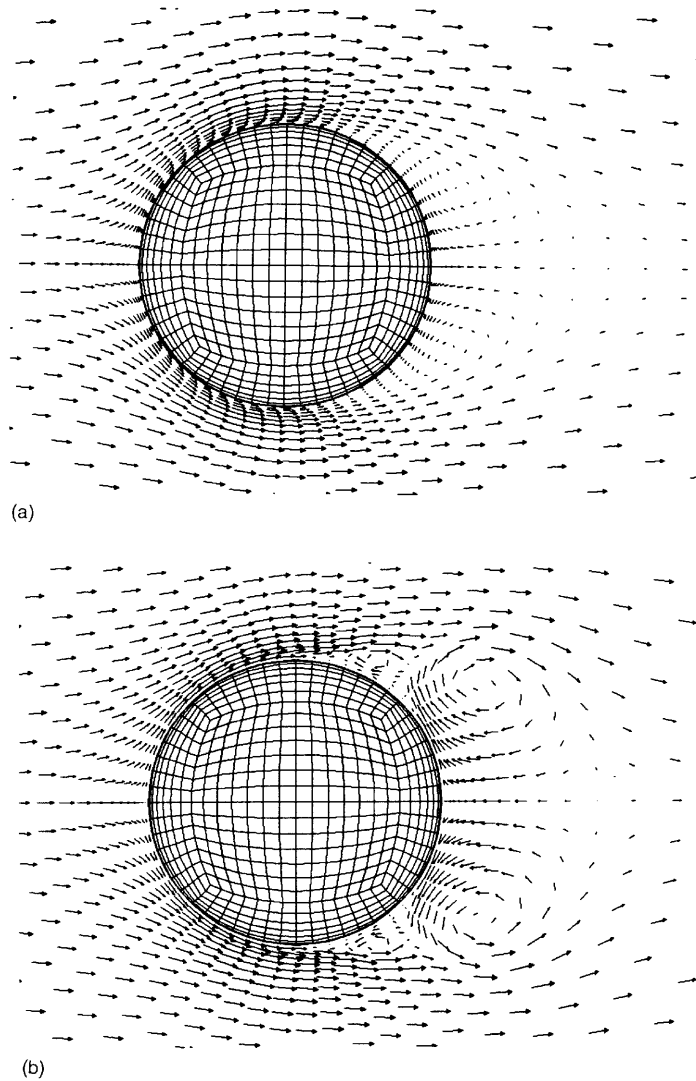
Figure 6. Velocity vectors obtained with (a) first- and (b) second-order schemes at symmetry plane at about time level $T = 4$.
$Re = 162,000$

(Figure 12(b)). A detailed picture of the wake obtained with the second-order scheme is shown in Figure 13, where the separation region obtained with the second-order scheme is twice as long as the separation region obtained with the first-order scheme. Also seen in Figure 12(b) is a small separation region at the bottom of the fuselage where there is an unfavourable pressure gradient. The first-order scheme cannot predict that separation region because of high artificial diffusion. The detailed picture of this unfavourable pressure region is provided in Figure 14 as streamlines of the second-order scheme.

The pressure distribution on the surface of the fuselage at the symmetry plane is given in Figure 15. According to this figure, the pressure values follow, in general, the same trend for both solutions;
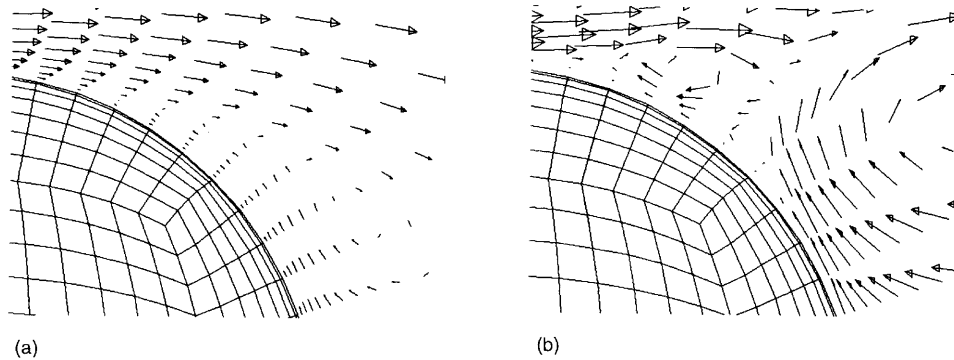
Figure 7. Velocity vector details on right shoulder of sphere on symmetry plane obtained with (a) first- and (b) second-order schemes. $Re = 162{,}000$

however, the unfavourable pressure gradient region at the bottom surface indicates where the two solutions do not agree.

Shown in Table III are the drag coefficient values for the sphere obtained with both schemes compared with the experimental data given in References 11–13. As can be seen, the first-order scheme slightly overestimates the coefficient value, whereas the second-order scheme estimates a value within the range of experimental values. These values are also plotted in Figure 3. The drag coefficient values evaluated for the helicopter fuselage with both schemes are also given in Table III.
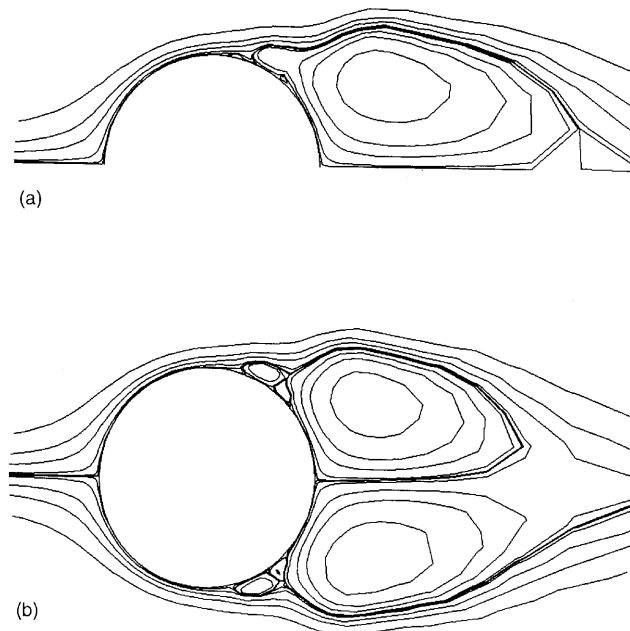
Figure 8. Calculated streamline patterns on (a) equatorial plane (x–z plane) and (b) symmetry plane (x–y plane) at dimensionless time level $T = 17$. $Re = 162{,}000$
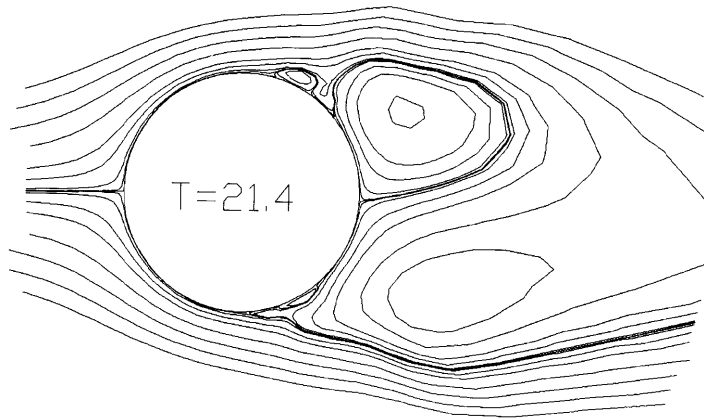
Figure 9. Natural start of vortex shedding (without any artificial disturbances) where streamlines are drawn at $T = 21 \cdot 4$ on symmetry plane (x–y plane). $Re = 162,000$
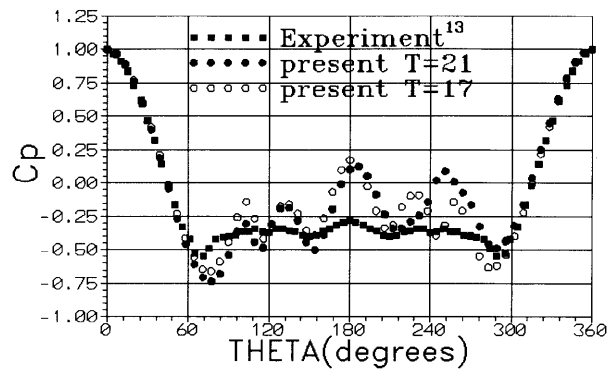

Figure 10. Comparison between calculated and experimental[13] surface pressure coefficient (C_p) distributions on symmetry plane. $Re = 162,000$

Table III. Drag coefficient vlaues for sphere and helicopter fuselage

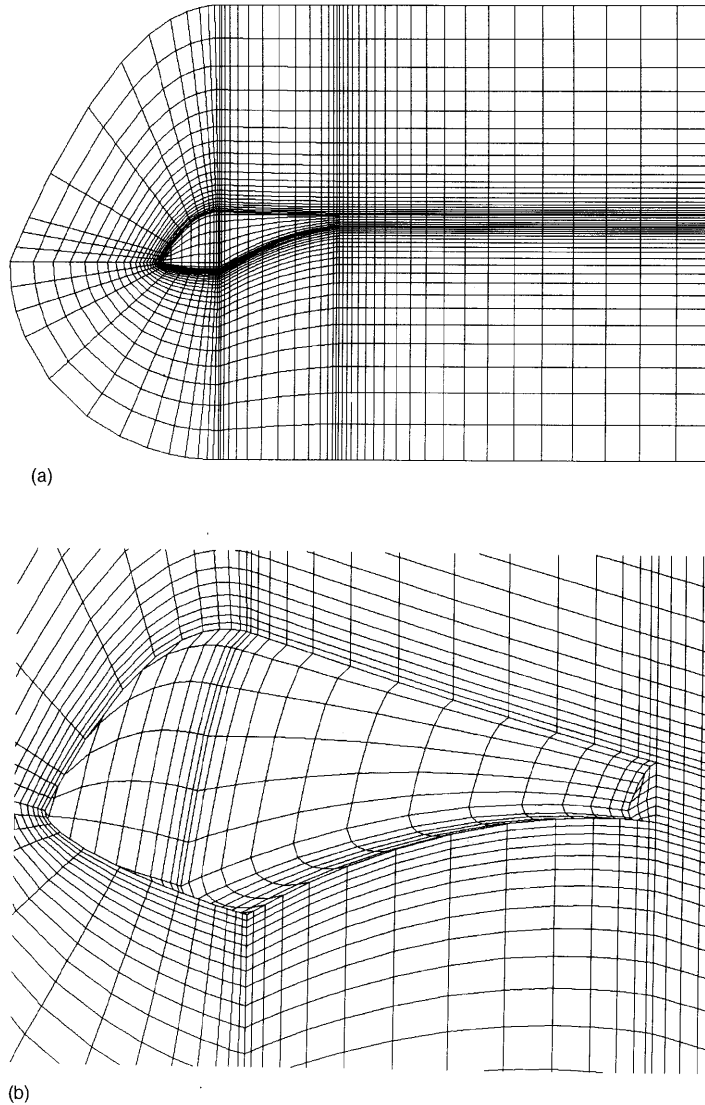| Geometry	Re	Scheme	C_D
Sphere	162000	Data[11–13]	0·12–0·51
		First-order	0·52
		Second-order	0·30
Fuselage	50000	First-order	0·20
		Second-order	0·11

Figure 11. (a) Grid on symmetry plane and (b) near-body details around helicopter fuselage; 11,280 brick elements with 12,915 nodes are used to resolve symmetric half of flow field

For all case studies the computations are performed on a computer equipped with an i860 processor. The average computation per time step per grid point takes approximately 0·0006 s of CPU time. The time steps used are between 0·003 and 0·01 depending on the minimum characteristic length of a brick element and the flow Reynolds number. This is to satisfy the stability criteria given in Reference 3.
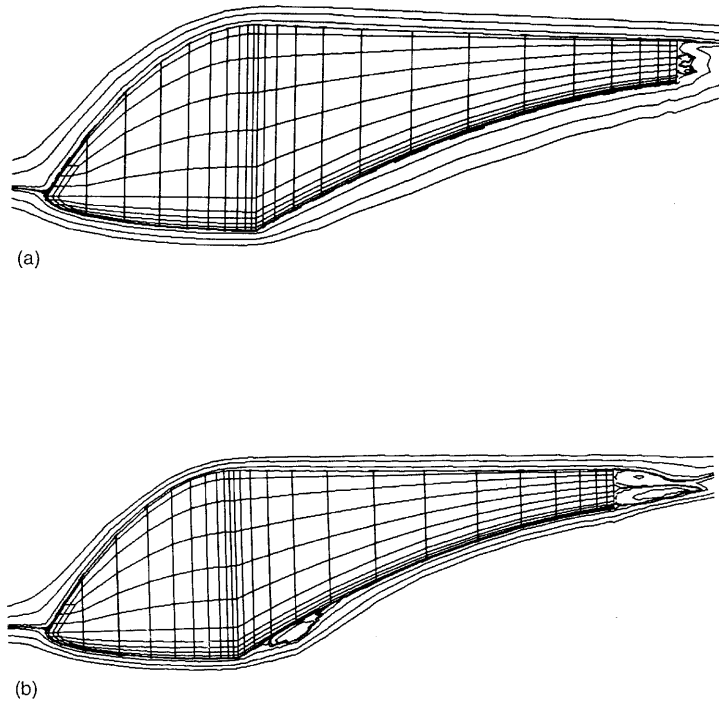
Figure 12. Symmetry plane streamlines at about steady state obtained with (a) first- and (b) second-order scheme. $Re = 50,000$
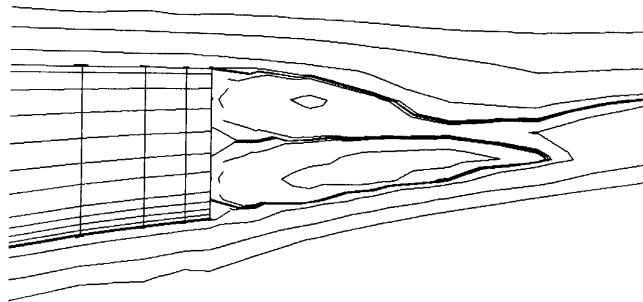

Figure 13. Details of separation bubble obtained with second-order scheme

4. CONCLUSIONS

A computer code based on a second-order-accurate scheme is developed and implemented for flows involving large separations and strong recirculations about arbitrary shapes. The accuracy achieved in time and space allows us to take large time steps using coarse grids.

The results obtained for various test cases are in good agreement with the existing numerical and experimental data.

The code is implemented satisfactorily to predict the drag coefficient of a generic helicopter fuselage.
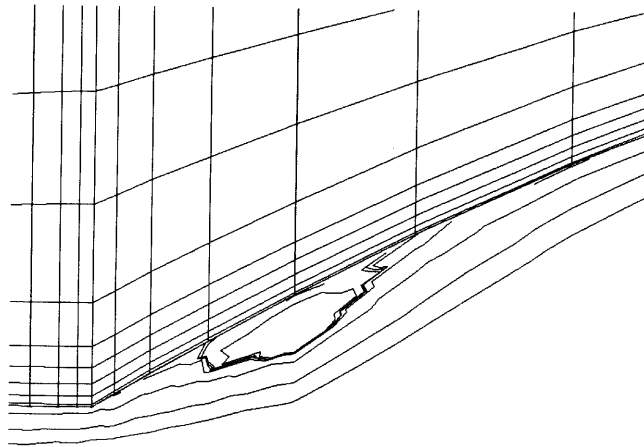
Figure 14. Detailed picture of unfavourable pressure region as streamlines of second-order scheme
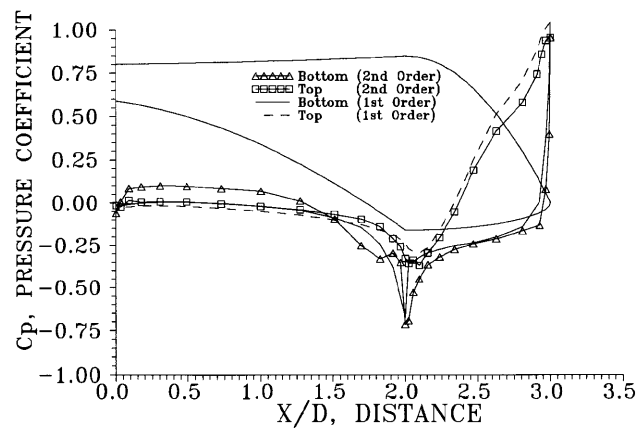

Figure 15. Pressure distribution (C_p) on surface of fuselage at symmetry plane. $Re = 50,000$

REFERENCES

1. T. J. R. Hughes, R. M. Ferencz and J. D. Hallquist, 'Large scale vectorized implicit calculations in solid mechanics on a Cray X-MP/48 utilizing EBE preconditioned conjugate gradients', *Comput. Methods Appl. Mech. Eng.*, **61**, 215–248 (1987).
2. M. P. Reddy, J. N. Reddy and H. U. Akay, 'A penalty finite element formulation using element-by-element solution strategy', *Comput. Methods Appl. Mech. Eng.*, **100**, 169–205 (1992).
3. Ü. Gülçat, 'An explicit FEM for 3-D general viscous flow studies based on E-B-E solution algorithms', *Comput. Fluid Dyn.*, **4**, 73–85 (1995).
4. H. C. Ku, R. S. Hirsch and T. D. Taylor, 'A pseudospectral method for solution of the three dimensional incompressible Navier–Stokes equations', *J. Comput. Phys.*, **70**, 439–462 (1987).
5. O. C. Zienkiewicz and R. L. Taylor, *The Finite Element Method*, Vol. 1, McGraw-Hill, London, 1989.

6. M. F. Webster and P. Townsend, 'Development of a transient approach to simulate Newtonian and non-Newtonian flow', *NUMETA '90, Numerical Methods in Engineering: Theory and Applications*, in G. N. Pande and J. Middleton (eds), Vol. 2, Elsevier, Oxford, 1992, pp. 1003–1012.
7. Y. Kallinderis and K. Nakajima, 'Finite element method for incompressible viscous flows with adaptive hybrid grids', *AIAA J.*, **32**, 1617–1625 (1994).
8. Ü. Gülçat, A. R. Aslan and A. Mısırlıoğlu, 'Aerodynamics of fuselage and store–carriage interaction using CFD', *Proc. AGARD 76th Fluid Dynamics Panel Symp. on Aerodynamics of Store Integration*, Ankara, April, 1995, paper 7.
9. A. R. Aslan, Ü. Gülçat and A. Misirlioğlu, 'A PCG/E-B-E iteration for high order and fast solution of 3-D Navier–Stokes equations', *Proc. AGARD 77th Fluid Dynamics Panel Symp. on Progress and Challenges in CFD Methods and Algorithms*, Seville, October 1995.
10. Y. Rimon and S. I. Cheng, 'Numerical solution of a uniform flow over a sphere at intermediate Reynolds numbers', *Phys. Fluids*, **12**, 949–959 (1969).
11. S. W. Churchill, *Viscous Flows, the Practical Use of Theory*, Butterworths, 1972, pp. 360–400.
12. B. Cantaloube, K. C. Le Thanh and Y. Morchoisne, 'Multidomain technique for 3-D incompressible unsteady viscous flow', in G. N. Pande and J. Middleton (eds), *NUMETAV90, Numerical Methods in Engineering: Theory and Applications*, Vol. 2, Elsevier, Oxford, 1990, pp. 914–923.
13. E. Achenbach, 'Experiments on the flow past spheres at very high Reynolds numbers', *J. Fluid Mech.*, **54**, 565–575 (1972).